

# Electron-ion Recombination of Fe XII forming Fe XI: Laboratory Measurements and Theoretical Calculations

O. Novotný<sup>1</sup>, N. R. Badnell<sup>2</sup>, D. Bernhardt<sup>3</sup>, M. Grieser<sup>4</sup>, M. Hahn<sup>1</sup>, C. Krantz<sup>4</sup>,  
M. Lestinsky<sup>1,5</sup>, A. Müller<sup>3</sup>, R. Repnow<sup>4</sup>, S. Schippers<sup>3</sup>, A. Wolf<sup>4</sup>, and D. W. Savin<sup>1</sup>

oldrich.novotny@mpi-hd.mpg.de

July 23, 2018

## ABSTRACT

We have measured electron-ion recombination for Fe XII forming Fe XI using a merged beams configuration at the heavy-ion storage ring TSR located at the Max Planck Institute for Nuclear Physics in Heidelberg, Germany. The measured merged beams recombination rate coefficient (MBRRC) for collision energies from 0 to 1500 eV is presented. This work uses a new method for determining the absolute MBRRC based on a comparison of the ion beam decay rate with and without the electron beam on. For energies below 75 eV, the spectrum is dominated by dielectronic recombination (DR) resonances associated with  $3s \rightarrow 3p$  and  $3p \rightarrow 3d$  core excitations. At higher energies we observe contributions from  $3 \rightarrow N'$  and  $2 \rightarrow N'$  core excitations DR. We compare our experimental results to state-of-the-art multi-configuration Breit-Pauli (MCBP) calculations and find significant differences, both in resonance energies and strengths. We have extracted the DR contributions from the measured MBRRC data and transformed them into a plasma recombination rate coefficient (PRRC) for temperatures in the range of  $10^3$  to  $10^7$  K. We show that the previously recommended DR data for

---

<sup>1</sup>Columbia Astrophysics Laboratory, Columbia University, New York, NY 10027, USA

<sup>2</sup>Department of Physics, University of Strathclyde, Glasgow G4 0NG, UK

<sup>3</sup>Institut für Atom- und Molekülphysik, Justus-Liebig-Universität Giessen, D-35392 Giessen, Germany

<sup>4</sup>Max Planck Institute for Nuclear Physics, 69117 Heidelberg, Germany

<sup>5</sup>Present address: GSI Helmholtzzentrum für Schwerionenforschung mbH, D-64291 Darmstadt, Germany

Fe XII significantly underestimate the PRRC at temperatures relevant for both photoionized plasmas (PPs) and collisionally ionized plasmas (CPs). This is to be contrasted with our MCBP PRRC results which agree with the experiment to within 30% at PP temperatures and even better at CP temperatures. We find this agreement despite the disagreement shown by the detailed comparison between our MCBP and experimental MBRRC results. Lastly, we present a simple parameterized form of the experimentally derived PRRC for easy use in astrophysical modelling codes.

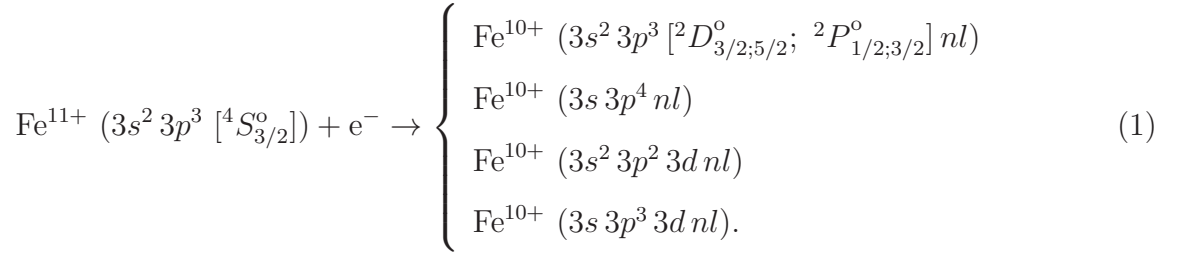
*Subject headings:* atomic data — atomic processes — galaxies: active — galaxies: nuclei — plasmas — X-rays: galaxies

## 1. Introduction

Iron M-shell ions have been identified as the dominant source of the 15–17 Å absorption feature seen in *Chandra* and *XMM-Newton* X-ray observations of warm absorbers in active galactic nuclei (AGNs; e.g., Sako et al. 2001, Holczer et al. 2010). This feature can be used to diagnose the properties of AGNs (Behar et al. 2001). Such a study, however, requires reliable low temperature dielectronic recombination (DR) rate coefficients for iron M-shell ions, as has been discussed by Netzer (2004), Kraemer et al. (2004), Chakravorty et al. (2008), and Kallman (2010).

A series of experimental and theoretical studies has been performed to meet this need (Gu 2004; Badnell 2006a,b; Altun et al. 2006, 2007; Schmidt et al. 2006, 2008; Lukić et al. 2007; Lestinsky et al. 2009). The measurements in this series are based on a storage ring merged beams technique utilizing the TSR heavy ion storage ring located at the Max-Planck-Institute for Nuclear Physics in Heidelberg, Germany (Habs et al. 1989). A bibliographic compilation of storage ring DR measurements for astrophysically relevant ions has recently been given by Schippers (2009) and an overview of TSR experiments on Fe ions is given by Schippers et al. (2010).

As part of this effort, here we present new experimental results for P-like Fe XII forming S-like Fe XI. Throughout the rest of this paper recombining systems are identified by their initial charge state. The most relevant channels for DR of Fe XII are



The incident electron is captured into a Rydberg level with a principal quantum number denoted by  $n$ . DR proceeds via excitation of a core electron with a principal quantum number which we denote by  $N$ . The energies of the core excitations corresponding to  $\Delta N = N' - N = 0$  DR are listed in Table 1. Fe XII is predicted to form at plasma temperatures of  $\log T_e(\text{K}) \sim 4.76 - 5.48$  in photoionized gas (Kallman 2010) and  $\sim 5.87 - 6.25$  in collisionally ionized gas (Bryans et al. 2006, 2009) where  $T_e$  is the electron temperature in Kelvin.

The remainder of this paper is organized as follows: Section 2 gives a brief summary of the theoretical calculations. Section 3 describes the experimental setup used here. Our experimental results for the merged beams recombination rate coefficient (MBRRC) are presented and compared to theory in Section 4. Section 5 reports our experimentally-derived DR plasma recombination rate coefficient (PRRC), a comparison with theory, and a simple fitting formula for plasma modeling. Lastly, a summary is given in Section 6.

## 2. Theory

The partial, energy averaged, DR cross section  $\bar{\sigma}_{fi}^z$  from an initial state  $i$  of an ion  $X^{+z}$  into a resolved final state  $f$  of an ion  $X^{+z-1}$  is given in the isolated resonance approximation

by (Burgess 1964; Badnell 2006a)

$$\bar{\sigma}_{fi}^z(E_c) = \frac{2\tau_0(\pi a_0 I_H)^2}{E_c \Delta E} \sum_j \frac{\omega_j}{\omega_i} \frac{\sum_l A_{j \rightarrow i, E_c l}^a A_{j \rightarrow f}^r}{\sum_h A_{j \rightarrow h}^r + \sum_{m, l} A_{j \rightarrow m, E_c l}^a}. \quad (2)$$

Here  $\omega_j$  is the statistical weight of the doubly-excited resonance state  $j$  in the recombined  $+z - 1$  ion,  $\omega_i$  is the statistical weight of the initially state of the initial  $+z$  ion, and the autoionization ( $A^a$ ) and radiative ( $A^r$ ) rates are in inverse seconds. The indices  $h$  and  $m$  are for states in the  $+z - 1$  and  $+z$  ions, respectively.  $E_c$  is the energy of the incoming continuum electron (with orbital angular momentum  $l$ ) which is fixed by the position of the resonances,  $\Delta E$  is an arbitrary bin width,  $I_H$  is the ionization potential energy of the hydrogen atom,  $\tau_0$  is the atomic unit of time, and  $a_0$  is the Bohr radius.

We use the general atomic collision code AUTOSTRUCTURE (Badnell 1986, 2006a, 2011) to calculate the constituents of Equation 2. The calculations for  $\Delta N = 0$  core-excitations were carried out in intermediate coupling using a configuration interaction expansion for the  $\text{Fe}^{11+}$  15-electron target involving a Ne-like core and valence configurations of  $3s^2 3p^3$ ,  $3s 3p^4$ ,  $3s^2 3p^2 3d$ ,  $3p^5$ ,  $3s 3p^3 3d$ ,  $3s^2 3p 3d^2$ ,  $3p^4 3d$ , and  $3s 3p^2 3d^2$  to which continuum and Rydberg electron orbitals were coupled. The 16-electron configurations, formed by adding a  $3s$ ,  $3p$ , or  $3d$  orbital to the 15-electron configurations, were included to describe outer electron radiative transitions into the core. Radiative transitions from higher  $n$  levels were described hydrogenically. The merged beams experiment does not resolve the final state and so all of the results that we present are for the total recombination cross section, i.e., summed over all  $f$  that are stable against autoionization and are not field ionized in TSR before they are detected. These energy-averaged cross sections can be convolved with the experimental energy distribution for comparison with the measurements. They can also be convolved with a Maxwellian distribution for modelling use and summed over all possible stable final states to generate a total PRRC. For  $\Delta N = 0$  DR, the sum over the Rydberg  $nl$  states extended to  $n = 1000$  and  $l = 11$  for the total Maxwellian rate coefficients while

for comparison with experiment the relevant survival probabilities were folded into the sum over the final-states (e.g., Schippers et al. 2001).

The contributions from  $\Delta N > 0$  core-excitations were also calculated by `AUTOSTRUCTURE` but using a configuration-averaged approximation (Pindzola et al. 1986). This approximation is only suited for  $\Delta N > 0$  Maxwellian rate coefficients since it only resolves resonance positions and channels by configuration only. The omission of configuration mixing is not a severe one for the total PRRC given that mixing conserves the overall amount of resonance strengths and, at the energies relevant here, causes only small fractional errors in the resonance energies (Badnell et al. 2011). We include both  $N = 2 \rightarrow 3$  and  $N = 3 \rightarrow 4$  core excitations. The sum over the captured electron  $nl$  Rydberg states extended to  $n = 100$  and  $l = 6$  for these total Maxwellian rate coefficients. No difference is seen between the calculations with and without the field ionization effects included.

### 3. Experimental Setup

#### 3.1. General

Measurements were performed using the heavy-ion storage ring TSR. Details on the various aspects of the merged beam technique as used at TSR have been described at length by Kilgus et al. (1992), Lampert et al. (1996), Pastuszka et al. (1996), Schippers et al. (2001), Wolf et al. (2006), Lestinsky et al. (2008), Schmidt et al. (2008) and Lestinsky et al. (2009). Here we discuss only those aspects particular to the present work.

A 150 MeV beam of  $^{56}\text{Fe}^{11+}$  was generated by first passing  $^{56}\text{Fe}^-$  ions through a carbon foil to strip and produce the desired charge state and then further accelerating them. After charge-to-mass selection, the  $\text{Fe}^{11+}$  beam was injected into the storage ring. Ions were accumulated by multi-turn injection and “e-cool stacking” (Grieser et al. 1991). Typical

stored ion currents were  $\sim 1 - 2 \mu\text{A}$  during data acquisition with storage times of  $\approx 10$  s.

Ions produced by foil-stripping can be highly excited (Martinson & Gaupp 1974). Here we stored the ions for  $\sim 1.5 - 2.0$  s before beginning data acquisition. We used a numerical model of the radiative decay process to determine the level populations in the ion beam after this initial storage time. The model considered excited states up to the  $3s^2 3p^2 4d^2 S_{1/2}$  level and included all 66 transitions, involving 31 levels, for which radiative rates are given in the ASD/NIST database (Ralchenko et al. 2011). These data, in turn, come from Fawcett et al. (1972), Huang (1984), and Shirai et al. (1990). The initial relative populations of the excited states were modelled using a Boltzmann distribution with a temperature of  $k_{\text{B}}T = 750$  eV. This corresponds to the approximate collision energy of the foil electrons as the  $\text{Fe}^-$  ions passed through the carbon foil. After 1.5 s of storage, over 98.5% of the ion beam is expected to be in the ground state. A factor of 10 increase or decrease in the effective temperature has an insignificant effect on this estimate. The most critical lifetime determining the final population is that of the  $3s^2 3p^3 [^2D_{5/2}^o] \rightarrow 3s^2 3p^3 [^4S_{3/2}^o]$  radiative transition to the ground state. The Einstein coefficient listed in ASD/NIST database at  $1.84 \text{ s}^{-1}$  is smaller compared to the more recent experimental value of  $3.26 \text{ s}^{-1}$  reported by Träbert et al. (2002). Using the latter result, the predicted ground state population after 1.5 s of storage is 99.0%. For both lifetimes, the ground state population averaged over the entire  $\sim 20$  s storage time is greater than 99.9%.

TSR is equipped with two different electron beam devices located in separate sections of the ring. Each electron beam can be merged to co-propagate with the stored ions. One of the devices is called the Cooler (Steck et al. 1990) and the other the Target (Sprenger et al. 2004). Either or both of the electron beams can serve to reduce the energy spread of the ions, i.e., to cool the ions. Electron cooling (Poth 1990) results in a narrow ion beam diameter ( $< 1$  mm) with a low energy spread. Additionally, either one of the electron beams can be

used as an interaction medium while the other continues to cool the ion beam. Electron-ion collisions can then be investigated by varying the energy of one of the electron beams.

The electron beam energy spread is described by a flattened Maxwellian distribution characterized by the longitudinal and transverse temperatures  $T_{\parallel}$  and  $T_{\perp}$  (Kilgus et al. 1992). At a collision energy of  $\hat{E}$ , the corresponding center-of-mass collision energy resolution  $\Delta\hat{E}$  is approximately given by  $\Delta\hat{E} = [(\ln(2)k_{\text{B}}T_{\perp})^2 + 16\ln(2)\hat{E}k_{\text{B}}T_{\parallel}]^{1/2}$  (Müller 1999). The Cooler uses a thermionic emission cathode. Typical electron beam temperatures are  $k_{\text{B}}T_{\parallel}^{\text{c}} \approx 180 \mu\text{eV}$  and  $k_{\text{B}}T_{\perp}^{\text{c}} \approx 13.5 \text{ meV}$  (Lestinsky et al. 2008). The Target uses a photocathode (Pastuszka et al. 2000; Orlov et al. 2004). From this we produce a beam with significantly lower temperatures of  $k_{\text{B}}T_{\parallel}^{\text{t}} \approx 25 \mu\text{eV}$  and  $k_{\text{B}}T_{\perp}^{\text{t}} \lesssim 1.5 \text{ meV}$  (Lestinsky et al. 2008). The complexity of the  $\text{Fe}^{11+}$  DR spectrum prevented direct determination of the Cooler and Target temperatures from the measured spectrum. Hence, for the results presented here we used values from a similar experiment (Lestinsky et al. 2008).

The products of charge-changing reactions are deflected from the parent ion beam by the first dipole magnet downstream of each electron beam device and are directed onto a detector. Scintillator detectors for measuring recombination are located after both the Cooler and the Target (Miersch et al. 1996; Wissler 2002; Lestinsky 2007). To measure electron impact ionization (EII), we used a converter plate coupled with a channel electron multiplier (CEM; Rinn et al. 1982; Linkemann et al. 1995) located after the Cooler. The recombination and ionization signals were used to determine the absolute recombination rate coefficient from the ion beam lifetime as described below.

The efficiency of each detector, in the absence of dead time effects, is essentially 100%. The dead time for each detector was estimated from the maximal width of the electronic pulses. This was shorter than 100 ns in all cases. As the count rates never exceeded 300 kHz, the corresponding dead time corrected detector efficiency did not decrease below 97%.

Field ionization of the recombined ions in the dipole magnet can ionize electrons captured into Rydberg levels with  $n \geq n_{\text{cut}}$ . A semi-classical calculation yields  $n_{\text{cut}} = 42$ . However, during the travel time from the interaction region to the dipole, some of the initially high Rydberg states can radiatively decay below  $n_{\text{cut}}$  and avoid ionization in the magnet. Schippers et al. (2001) have derived a model to calculate  $nl$ -specific detection probabilities taking into account the field ionization and radiative de-excitation processes. The average Rydberg state cut-off resulting from this model is  $n_{\text{cut}} \approx 54$ . For comparison of our results to the theory we use the detection probabilities provided by this model.

### 3.2. Determination of the relative MBRRC spectra

Normally the absolute MBRRC is derived from the measured recombination counts using an appropriate normalization to the electron density and ion current (e.g., Schmidt et al. 2008). The electron density can be readily measured accurately (e.g., Lestinsky et al. 2009). However, here the average stored ion current of  $\sim 1 - 2 \mu\text{A}$  in the present experiment was too low to be directly measured using the DC current transformer installed in the ring. Instead, a relative MBRRC was determined by normalizing the signal count rate to a proxy for the ion current. For this we used the relative intensity of the ion beam as recorded by a beam profile monitor (Hochadel et al. 1994). To derive the absolute calibration of the MBRRC spectrum we use the approach described in Section 3.3.

Data were collected for electron beam laboratory energies from  $\approx 1450 - 6000 \text{ eV}$ . These translate to center-of-mass collision energies  $0 \leq \hat{E} \leq 1500 \text{ eV}$ , where  $\hat{E} = 0$  corresponds to matched electron and ion beam velocities. The full range was covered using the Cooler to collect data with continuous cooling by the Target. The high electron beam density of  $n_e \approx 2.7 \times 10^7 \text{ cm}^{-3}$  in the Cooler allowed for shorter data acquisition times than that of the Target which had a density of  $n_e \approx 1.1 \times 10^6 \text{ cm}^{-3}$ . The roles were reversed to cover the



low energy range  $0 \leq \hat{E} \leq 0.2$  eV at the higher energy resolution offered by the Target. As discussed in Section 4, these data aided in the extraction of the low energy DR resonance strengths needed to generate a reliable low temperature PRRC.

Each data run lasted  $\sim 1 - 2$  hrs, during which time we continuously repeated the measurement cycle of ion injection, cooling, and data acquisition. During data collection the electron beam energy was stepped between a variable *measurement* energy and a fixed *reference* energy, creating  $\sim 350$  measurement pairs of typically  $\lesssim 20$  s total duration. The measurement energy was changed after each reference step. For each data run the measurement energy range in the laboratory frame spanned over  $\sim 140 - 1000$  eV. This is much smaller than the total laboratory energy range studied. The reason for splitting to smaller energy ranges is related to the required settling time of the power supplies when switching the electron beam laboratory energy to measurement or reference. In order to keep this time short (15 ms in our case), the reference laboratory energy in each run was kept close to the measurement laboratory energy range. As a result, several data runs were needed to cover the entire laboratory energy range measured. After the 15 ms settling time, the subsequent dwell time at each measurement or reference energy step was 10 – 25 ms.

The signal at reference consists of background due to electron capture from residual gas, radiative recombination (RR), and potentially also DR. At high energies DR is negligible and so when we subtracted the reference from the measurement it was only necessary to re-add the small theoretical RR contribution, thereby insuring that only the appropriate background was subtracted. In the low energy runs, however, the DR contribution at the reference energy became non-negligible. We corrected for this by comparing a lower energy run to an overlapping higher energy run and shifting the offset in the former to match the data in the latter.

### 3.3. Absolute scaling of MBRRC spectra

We put our relative MBRRC results on an absolute scale using measurements of the ion beam lifetime with the Cooler electron beam first *off* and then *on*. A similar normalization method has been used for molecular ion studies (Pedersen et al. 2005). Our approach builds upon and extends their work.

With the Cooler off, the ion beam decays exponentially due to collisions with the residual gas along the entire TSR circumference. The measured storage lifetime  $\tau^{\text{off}}$  is inversely proportional to the loss rate  $\lambda_{\text{res}}^{\text{off}}$  as

$$\frac{1}{\tau^{\text{off}}} = \lambda_{\text{res}}^{\text{off}}. \quad (3)$$

With the Cooler on at a fixed energy  $\hat{E}$ , the measured storage lifetime is now due to both collisions with the residual gas and also to RR and DR in the Cooler giving

$$\frac{1}{\tau^{\text{on}}} = \lambda_{\text{res}}^{\text{on}} + \hat{\alpha} n_e \eta. \quad (4)$$

Here  $\lambda_{\text{res}}^{\text{on}}$  is the residual gas collisional loss rate with the Cooler on,  $\hat{\alpha}$  is the RR+DR MBRRC at  $\hat{E}$ ,  $n_e$  is the Cooler electron density, and  $\eta = L/C$  is the overlap length  $L$  of the ion and electron beams normalized by the total storage ring circumference  $C$ . As a first approximation, we set  $\lambda_{\text{res}}^{\text{off}} = \lambda_{\text{res}}^{\text{on}}$  and solve Equations 3 and 4 to yield an absolute MBRRC

$$\hat{\alpha}(\hat{E}) = \frac{1}{n_e \eta} \left( \frac{1}{\tau^{\text{on}}} - \frac{1}{\tau^{\text{off}}} \right). \quad (5)$$

A more thorough derivation, accounting for the slight differences between  $\lambda_{\text{res}}^{\text{off}}$  and  $\lambda_{\text{res}}^{\text{on}}$  due to changes in the pressure of residual gas, is given in Appendix A. Here, this difference results in less than a 5% change in  $\hat{\alpha}(\hat{E})$ . The relative MBRRC results of Section 3.2 can then be put on an absolute scale by adjusting the data so that the value at  $\hat{E}$  matches the absolute rate derived using this lifetime method.

Figure 1 shows an example of data collected using this method for matched ion and electron beam velocities ( $\hat{E} = 0$  eV). For these results, the ions were cooled for 3 s after

injection and then the Cooler beam switched off. Some time later the Cooler beam was switched back on. The relative beam intensity for each phase was monitored by detecting products from ion collisions resulting in electron capture and ionization. We determined the beam lifetime using the decaying signal strength on both the recombination and ionization detectors. For the results presented here the Target electron beam was on continuously.

For the present work the measured beam lifetime decreased dramatically when the Cooler was turned on due to the extraordinary high rate coefficient of DR+RR at  $\hat{E} = 0$  which dominates over collisions with the residual gas at the given electron density. This can be seen in both the recombination and ionization detector count rates shown in Figure 1. The Cooler energy is below the Fe XII threshold for electron impact ionization ( $\sim 330$  eV, Ralchenko et al. 2011) and so the signal on the ionization detector originated exclusively from electron stripping in ion collisions with residual gas. Thus, we attribute the small increase seen in the ionization product count rate when the Cooler is turned on as being due to a corresponding increase in the residual gas pressure. This pressure change is accounted for in our analysis as is described in Appendix A and has less than a 5% effect on our results. We also found that, to within the statistical errors, the absolute scaling method used here gave the same results independent of when the Cooler was switched on or whether the Target was on or off.

We use the absolute MBRRC results to scale our relative MBRRC data. These are then corrected for the effects due to the merging and demerging of the electrons with the ions (Lampert et al. 1996). This correction largely removes errors due to the uncertainty in the exact electron-ion beams overlap length.

### 3.4. Uncertainties

The  $1\sigma$  statistical error in our rate coefficient data is about 1% for collision energies below 1 meV. As the energy increases, the recombination rate, and hence the signal rate, decreases. This leads to an increase in the statistical error with increasing energy. It remains below 5% for energies up to 66 eV and  $\sim 7\%$  for 66 – 1500 eV.

We treat the various systematic errors in our measurement as uncorrelated and add them in quadrature. The resulting  $1\sigma$  systematic error is estimated to be 12%, 13%, and 40% for collision energies of 0 eV, 66 eV, and above 66 eV, respectively. Here we briefly review the sources of the total systematic uncertainty. Further details about systematic errors can be found in the TSR references cited in Sec. 3.1.

The largest source of systematic error below 66 eV is due to the electron density determination. The unusually high 10% error for the data here resulted from the accidental use of a degraded photocathode for the absolute MBRRC measurement. The reproducibility of the absolute results and the extraction of ion beam lifetimes for the determination of the absolute MBRRC at 0 eV result in an additional 5% uncertainty.

The data have been stitched together going from high to low energies to correct for the changing reference energy. As the data have been normalized at  $\hat{E} = 0$ , this stitching results in a 5% error at 66 eV and up to a 35% error at higher energies. The large increase in this error above 66 eV is due to the  $\sim 100$  times decrease in the magnitude of the MBRRC. Other remaining sources of error include the corrections for the merging and demerging of the beams (1%; Lampert et al. 1996) and the deadtime counting efficiencies of detectors.

#### 4. Merged beams recombination rate coefficient

The measured MBRRC data are displayed in Figures 2 and 3 for the energy ranges 0 – 80 eV and 65 – 1500 eV, respectively. These data were acquired using the Cooler as the probe beam and the Target for cooling. Also shown are our AUTOSTRUCTURE MCBP results, with and without the experimental field ionization effects. The theoretical cross section has been multiplied by the collision velocity and convolved with the Cooler energy spread to generate a theoretical MBRRC.

The Fe XII resonance spectrum for this system with a half open  $p$ -shell is very rich and challenging to disentangle. In general the features are broad and unresolved making individual assignments essentially impossible. DR via  $3s^23p^3$  intra-configuration core excitations is expected for energies below  $\approx 10$  eV. The bulk of these contribute significantly only below  $\approx 5$  eV as can be seen by the step-like drop in the MBRRC at this energy. Moving up in energy, most of the  $3s3p^4$  core excitations are expected to occur below  $\approx 35$  eV. At energies of 35 – 75 eV, the features become more regular. These are due largely to  $3s^23p^23d$  core excitations and the resonances can be more easily assigned. For clarity we have labeled only those resonances which are due to the strongest  $3s3p^4$  and  $3s^23p^23d$  series. Filling in the many other resonances series would make the figures too cluttered for meaningful inspection.

Given the complexity of the spectra, for comparison with theory we have followed Lestinsky et al. (2009) and calculated

$$\kappa = \frac{\int \alpha_{\text{theo}}^{\text{DR}} dE}{\int \alpha_{\text{exp}}^{\text{DR}} dE} \quad (6)$$

for sequential energy ranges. The lowest energy considered is 13.5 meV to avoid the well known effects of enhanced RR near  $\hat{E} = 0$  (Gwinner et al. 2000; Wolf & Gwinner 2003; Hörndl et al. 2006). In the denominator of Equation 6 we take  $\alpha_{\text{exp}}^{\text{DR}} = \alpha_{\text{exp}} - \alpha_{\text{theo}}^{\text{RR}}$ . We have calculated  $\alpha_{\text{theo}}^{\text{RR}}$  using both the hydrogenic Bethe-Salpeter method (Hoffknecht et al. 2001)

and a hydrogenic quantum mechanical dipole approximation for low  $n$  and a semiclassical approach with Stobbe corrections for high  $n$  (Stobbe 1930). The difference in  $\alpha_{\text{theo}}^{\text{RR}}$  between the two methods is insignificant.

We find mixed agreement between theory and experiment. Results for  $\kappa$  are given in Table 2. If the difference were solely due to the estimated  $1\sigma$  experimental systematic error, we would expect this ratio to range between  $0.88 - 1.15$  and  $0.71 - 1.67$  for collision energies below and above 66 eV, respectively. In the energy range  $0.0135 - 0.45$  eV,  $\kappa$  is nearly one third. This is most likely due to incorrectly predicted resonance energies resulting from the well-known difficulty of calculating DR resonance positions at low energies (cf., Schippers 2009 and Schippers et al. 2010 and references therein). In the various energy ranges between 0.45 eV and 46.0 eV, theory is smaller by more than the  $1\sigma$  experimental systematic uncertainty. Reasonable agreement is found in the range  $46 - 53$  eV. However in the range  $53 - 59$  eV, theory is 1.4 times greater than experiment. This apparent systematic overestimate of the integrated theoretical resonance strength occurs for  $\Delta N = 0$  DR where the radiative stabilization is primarily by the core electron and the Rydberg electron occupies  $n \gtrsim 10$ . Similar discrepancies have been seen in previous work (Lestinsky et al. 2009) and are discussed in more detail by Lestinsky et al. (in preparation). The range  $59 - 66$  eV includes six Rydberg series, mostly with a  $3s^23p^23d$  configuration, and the large  $\kappa$  might be partly explained by uncertainties in the model for the experimental field ionization effect. Lastly, the range  $66 - 75$  eV covers ten Rydberg series limits associated with the  $3s^23p^23d$  configuration. The cause of the low  $\kappa$  here is unclear.

The MBRRC at energies above 75 eV is dominated by  $\Delta N > 0$  DR. Here the MBRRC is  $\sim 100$  times weaker than for  $\Delta N = 0$  at lower energies. Not surprisingly, our configuration averaged calculations do a poor job of reproducing the observed resonance structure. Between  $\sim 75 - 330$  eV the spectrum is expected to be dominated by DR via  $3 \rightarrow N'$  core excitations

where  $N' \geq 4$ . The resonances between  $\sim 75 - 217$  eV we attribute to  $3 \rightarrow 4$  excitations and the region between  $\sim 217$  eV and the ionization limit of excitations into  $N' \geq 5$ . In this first range, we find  $\kappa = 0.68$ . We cannot determine  $\kappa$  for the  $217 - 330$  eV range as the  $N' \geq 5$  resonances were not included in the theoretical model. The small decrease in the DR signal at  $\sim 330$  eV corresponds to the  $N = 3$  ionization threshold (Ralchenko et al. 2011). The next range from  $\sim 330 - 855$  eV is dominated by DR via  $2 \rightarrow N$  core excitations where  $N' \geq 3$ . We attribute the resonances seen in this range mainly to  $2 \rightarrow 3$  excitations and calculate a  $\kappa$  of 0.28. For the range  $\sim 855 - 1073$  eV, no theoretical data exists and we are unable to determine  $\kappa$ . The  $2 \rightarrow N'$  channels cease to contribute to DR once ionization from the  $N = 2$  level becomes possible at 1073 eV (Kaastra & Mewe 1993), as is readily visible in the measured data. It is worth noting, too, that a significant amount of the measured DR flux above  $\sim 60$  eV is not accounted for in the theoretical calculations.

We have also measured the MBRRRC using the Target as the probe beam and the Cooler for cooling. These results are shown in Figure 4 along with the data collected using the Cooler. The differences seen below 0.001 eV are attributed to enhancements in the RR signal as we discuss in Section 5. At higher energies, the greater resolution of the Target compared to the Cooler allows additional resonance features to be resolved, particularly for collision energies between 0.001 eV and 0.02 eV. Note also how the Target data drop to the level of the RR background around 0.03 eV. In Section 5 these Target results are used to determine the contribution of the low energy DR resonances to the PRRC.

## 5. Plasma DR rate coefficients

The derivation of the PRRC from the experimental MBRRRC data has been discussed in detail in Schippers et al. (2001, 2004), Schmidt et al. (2008), and Lestinsky et al. (2009). Four points need to be considered. First, at sufficiently high collision energies, the required

cross section can be extracted by dividing the MBRRC data by the classical relative velocity  $v_r = \sqrt{2\hat{E}/m_e}$ . For this we used the Cooler data shown in Figure 2.

Second, we need to account for recombination near various series limits into those levels which are expected to be field ionized in our experimental arrangement. Here we took the difference between the AUTOSTRUCTURE calculations with and without field ionization effects, scaled the difference by the  $\kappa$  factor for the energy range just below that where field ionization is an issue, and added the results to our measured MBRRC. The cross section was then extracted as described above.

Third, at lower energies (here  $\lesssim 0.11$  eV), the experimental energy spread becomes comparable to  $\hat{E}$ . Our approximation for the cross section breaks down and one must fit the data to extract resonance energies and strengths for the many unresolved resonances in the data. Here we used data collected with the Target as shown in Figure 4. The Target provides much higher resolution data for extracting resonances strengths compared to the Cooler data. The fitting procedure was described in detail by Schippers et al. (2004), Schmidt et al. (2008), and Lestinsky et al. (2009).

Lastly, at near zero energy, the RR signal may be experimentally enhanced (Gwinner et al. 2000; Wolf & Gwinner 2003; Hörndl et al. 2006). There may also be unresolved DR resonances. Previous work has shown that experimental enhancement of the RR MBRRC amounts to a factor of  $\sim 1.5 - 3$  as compared to that predicted by RR theory. Any remaining difference is attributed to unresolved DR resonances. As shown in Figure 4, the differences seen here at  $\sim 10^{-4}$  eV are a factor of  $\sim 360$  for the Cooler and  $\sim 420$  for the target. These factors strongly suggest the presence of unresolved low energy DR resonances. Also the fact that the slopes of the Target and Cooler DR data at  $\sim 10^{-3}$  eV differ significantly from those predicted by RR theory supports this hypothesis. We account for this likely DR when fitting our MBRRC data by including resonances at energies of 0.08 and



0.7 meV. We calculated the PRRC with and without these resonances. The average of the two PRRC results was used and half the difference between the two taken as the uncertainty. In this way we estimate the uncertainty due to the unclear origin of these resonances. This error was then propagated quadratically into the total error budget of the PRRC. However, the contribution of these resonances to the total PRRC is insignificant above  $10^3$  K which includes the temperatures where Fe XII is predicted to form in either photoionized or collisionally ionized gas (see Figure 5).

Taking all these points into account, we have derived the PRRC following the procedure laid out in Schippers et al. (2001, 2004), Schmidt et al. (2008), and Lestinsky et al. (2009). Figure 5 shows the results for Fe XII forming Fe XI in the temperature range of  $10^3 - 10^7$  K. The total uncertainty at an estimated  $1\sigma$  level reaches  $\lesssim 15\%$  at  $10^3$  K,  $\sim 15\%$  at  $10^5$  K,  $\sim 20\%$  at  $10^6$  K,  $\sim 27\%$  at  $2 \times 10^6$  K, and  $\sim 45\%$  at  $10^7$  K. Over the temperature range shown in the figure, the experimental DR PRRC is  $\gtrsim 35$  times larger than the theoretical RR value of Badnell (2006b).

The temperature ranges where the fractional abundance of Fe XII is  $\geq 1\%$  of the total Fe abundance in photoionized plasmas (PPs) and in collisionally ionized plasmas (CPs) are indicated in Figure 5 as grey shaded areas (Bryans et al. 2006, 2009; Kallman 2010). Also plotted is the previously recommended DR rate coefficient of Arnaud & Raymond (1992). These data significantly underestimate the DR PRRC at temperatures of below  $2 \times 10^5$  K, which are of particular importance for PPs. Also at temperatures relevant to CPs, their recommended DR data are up to about 2.4 times lower than our experimental results. Similar behavior has also been seen for other M-shell iron ions (Schmidt et al. 2006; Lukić et al. 2007; Schmidt et al. 2008; Lestinsky et al. 2009). The data reported by Arnaud & Raymond (1992) represent a compilation of theoretical calculations largely from the 1970s and 1980s. We attribute the differences seen, in part, to the limitation of computer power at that time

and the required approximations necessary to make the calculations tractable. More recent, state-of-the-art calculations have been performed by Badnell (2006b). However, these do not include DR via  $\Delta N > 0$  core excitations. We have extended those results by including DR via  $2 \rightarrow 3$  and  $3 \rightarrow 4$  core excitations. At PP temperatures both calculations are in significantly better agreement with experiment but still differ by up to 30% which is outside of the  $1\sigma$  experimental error bars. At CP temperatures both sets of theoretical results agree with experiment to within the experimental uncertainty, despite the significant disagreement between the MCBP theory and our experimental data on the MBRRC level (Figure 2). Obviously the averaging over the Maxwellian temperature distribution leads to a washing out of the discrepancies on the MBRRC level. Both the theoretical and experimental results indicate that  $\Delta N > 0$  channels contribute  $\geq 10\%$  to the PRRC at CP temperatures and up to 20% at  $10^7$  K.

To facilitate the use of our experimentally-derived PRRC in plasma models, we have parameterized the data using the function

$$\alpha_{\text{P}}^{\text{fit}}(T) = T^{-3/2} \sum_i c_i \exp(-E_i/T). \quad (7)$$

The fitted parameters  $c_i$  and  $E_i$  are listed in Table 3. The fit accurately reproduces the experimentally derived PRRC to better than 2% over the temperature range of  $10^3 - 10^7$  K.

## 6. Summary

We have measured the MBRRC for DR of Fe XII forming Fe XI over the collision energy range of 0 – 1500 eV. A merged electron-ion beams configuration was used at the TSR heavy ion storage ring. Poor agreement is found between the experimental and theoretical resonance structure, particularly for energies below  $\sim 35$  eV. Significant differences are also found for the integrated resonance strengths over most of the measured energy range. Similar

discrepancies between experiment and theory have been seen in our previous studies of DR for Fe M-shell ions (Schmidt et al. 2006; Lukić et al. 2007; Schmidt et al. 2008; Lestinsky et al. 2009).

From our experimental results we have derived a DR PRRC for plasma temperatures of  $10^3 - 10^7$  K. This range includes the temperatures where Fe XII is predicted to be abundant in photoionized and collisionally ionized cosmic plasmas, respectively. In general we see behavior similar to that noted for DR of other Fe M-shell ions (Schmidt et al. 2006; Lukić et al. 2007; Schmidt et al. 2008; Lestinsky et al. 2009). The previously recommended DR data of Arnaud & Raymond (1992) underestimate the DR PRRC by orders of magnitude at temperatures relevant for photoionized plasmas and by up to a factor of 2.4 for collisionally ionized gas. Much better agreement is found with state-of-the-art MCBP theory, though significant differences do remain at the lowest temperatures where modern theory is known to still have difficulties accurately predicting the energies of the relevant DR resonances.

We thank the accelerator and TSR group for their excellent support during the beam time. M.L., M.H., O.N. and D.W.S. were supported in part by the NASA Astrophysics Research and Analysis program and the NASA Solar and Heliospheric Physics Supporting Research program.

### **A. Lifetime based method for absolute scaling of MBRRC**

As discussed in Sec. 3.3, measurements for the lifetime of the stored ions with the Cooler *off* and *on* can be used to derive an absolute MBRRC. However, as a consequence of desorption from the surface of the vacuum chamber in the collector section, the residual gas pressure in the Cooler increases when the electron beam is turned on. Monitoring the pressure inside TSR by pressure gauges is not precise and local enough to describe such

increases. Here we explain how to account for these pressure changes without relying on direct pressure measurements.

Our measurements are performed on ground state  $\text{Fe}^{11+}$  at collision energies below the threshold for electron-impact ionization. Essentially the only electron-driven, charge-changing reaction which can occur under these conditions is electron-ion recombination. We estimate as insignificant the contributions from electron impact excitation to a bound level followed by an ionizing collision on the residual gas in the ring. The ion beam is also free of metastables, i.e., the beam composition does not change during measurements. The only other significant processes affecting the lifetime of the stored ions are collisions with residual gas particles in the ring leading to electron capture (recombination) or loss (ionization).

The Cooler energy is kept constant during the on-phase to insure that the electron collision rate coefficient to be derived is constant during measurement. Detectors downstream of the Cooler are used to monitor the various collision end-products. The other electron beam device in the ring needs to be continuously on or continuously off so as not to disturb the measurement. The derivation presented here assumes that the Target is on continuously. Also, although we collected data using the Cooler, the role of the Cooler and Target may be readily interchanged.

The rate coefficient for the electron-ion recombination is given by  $\alpha^1$ . The rate coefficients for this reaction in the Cooler (c) and Target (t) are generally not identical,  $\alpha_c^1 \neq \alpha_t^1$ , as each device has a different electron beam energy spread. Additionally, each device can be operated at different energies.

Collisions of the stored ions with the residual gas in the ring can result in either electron capture from the gas (1) or ionization (2) of the ions. Both processes affect the lifetime of the stored ions. Both are pressure dependent. In the following, the associated rate coefficients for charge capture and ionization are denoted as  $\beta^1$  and  $\beta^2$ , respectively.

We can readily write out expressions for the time  $t$  dependence of the number of stored ions in the ring  $N_i$ . With the Cooler off, this is given by

$$\frac{dN_i^{\text{off}}}{dt} = -N_i^{\text{off}} [(\beta^1 + \beta^2)\rho_c^{\text{off}}\eta_c + (\beta^1 + \beta^2)\rho_o^{\text{off}}(1 - \eta_c) + \alpha_t^1 n_t \eta_t]. \quad (\text{A1})$$

Here  $\eta_c$  and  $\eta_t$  are the fractions of the ring circumference covered by the Cooler and Target length, respectively,  $n_t$  is the Target electron density, and  $\rho_c$ ,  $\rho_o$  are the average residual gas densities in the Cooler (c) or in other sections of TSR (o). The “off” superscript is used to denote that the Cooler is off. With the Cooler on we have

$$\frac{dN_i^{\text{on}}}{dt} = -N_i^{\text{on}} [(\beta^1 + \beta^2)\rho_c^{\text{on}}\eta_c + (\beta^1 + \beta^2)\rho_o^{\text{on}}(1 - \eta_c) + \alpha_t^1 n_t \eta_t + \alpha_c^1 n_c \eta_c] \quad (\text{A2})$$

where the “on” superscript signifies the Cooler is on and  $n_c$  is the Cooler electron density. The solution for these equations is of the form

$$N_i^{\text{off/on}}(t) = N_{i,0}^{\text{off/on}} \exp(-t/\tau^{\text{off/on}}) \quad (\text{A3})$$

where  $N_{i,0}^{\text{off/on}}$  is the initial ion number and the ion beam lifetimes  $\tau^{\text{off/on}}$  are given by

$$(\tau^{\text{off}})^{-1} = (\beta^1 + \beta^2)\rho_c^{\text{off}}\eta_c + (\beta^1 + \beta^2)\rho_o^{\text{off}}(1 - \eta_c) + \alpha_t^1 n_t \eta_t \quad (\text{A4})$$

$$(\tau^{\text{on}})^{-1} = (\beta^1 + \beta^2)\rho_c^{\text{on}}\eta_c + (\beta^1 + \beta^2)\rho_o^{\text{on}}(1 - \eta_c) + \alpha_t^1 n_t \eta_t + \alpha_c^1 n_c \eta_c. \quad (\text{A5})$$

We can now readily solve for  $\alpha_c^1$  in terms of measured quantities. With the Cooler on and off, the count rates on detectors 1 (recombination) and 2 (ionization) at a time  $t$  are given by

$$R_c^{1,\text{on}}(t) = N_i^{\text{on}}(t)(\eta_c \alpha_c^1 n_c + \beta^1 \rho_c^{\text{on}} \eta_c) \quad (\text{A6})$$

$$R_c^{2,\text{on}}(t) = N_i^{\text{on}}(t)(\beta^2 \rho_c^{\text{on}} \eta_c) \quad (\text{A7})$$

$$R_c^{1,\text{off}}(t) = N_i^{\text{off}}(t)(\beta^1 \rho_c^{\text{off}} \eta_c) \quad (\text{A8})$$

$$R_c^{2,\text{off}}(t) = N_i^{\text{off}}(t)(\beta^2 \rho_c^{\text{off}} \eta_c). \quad (\text{A9})$$

Combining Equations A4 and A5 with Equations A6–A9 gives

$$\begin{aligned}
 (\tau^{\text{on}})^{-1} - (\tau^{\text{off}})^{-1} &= \frac{R_c^{1,\text{on}}(t) + R_c^{2,\text{on}}(t)}{N_i^{\text{on}}(t)} - \frac{R_c^{1,\text{off}}(t) + R_c^{2,\text{off}}(t)}{N_i^{\text{off}}(t)} \\
 &+ (\beta^1 + \beta^2)(\rho_o^{\text{on}} - \rho_o^{\text{off}})(1 - \eta_c). \tag{A10}
 \end{aligned}$$

Direct pressure measurements do not show significant pressure changes in TSR outside of the Cooler. Therefore we assume that the pressure in these sections is independent of the state of the Cooler beam and thus  $\rho_o^{\text{on}} = \rho_o^{\text{off}}$ . We take  $t_0$  as the time when the Cooler is switched on or off which gives  $N_i^{\text{on}}(t_0) = N_i^{\text{off}}(t_0) \equiv N_i(t_0)$ . Equation A10 thereby simplifies to

$$(\tau^{\text{on}})^{-1} - (\tau^{\text{off}})^{-1} = \frac{R_c^{1,\text{on}}(t_0) - R_c^{1,\text{off}}(t_0) + R_c^{2,\text{on}}(t_0) - R_c^{2,\text{off}}(t_0)}{N_i(t_0)}. \tag{A11}$$

Using Equations A6–A9 to solve for  $N_i(t_0)$  gives

$$N_i(t_0) = \frac{R_c^{1,\text{on}}(t_0) - R_c^{1,\text{off}}(t_0) R_c^{2,\text{on}}(t_0)/R_c^{2,\text{off}}(t_0)}{\eta_c \alpha_c^1 n_c}. \tag{A12}$$

Combining these last two equations we obtain

$$\hat{\alpha} \equiv \alpha_c^1 = \frac{(\tau^{\text{on}})^{-1} - (\tau^{\text{off}})^{-1}}{\eta_c n_c} \frac{R_c^{1,\text{on}}(t_0) - R_c^{1,\text{off}}(t_0) R_c^{2,\text{on}}(t_0)/R_c^{2,\text{off}}(t_0)}{R_c^{1,\text{on}}(t_0) - R_c^{1,\text{off}}(t_0) + R_c^{2,\text{on}}(t_0) - R_c^{2,\text{off}}(t_0)}. \tag{A13}$$

The measured values used to solve Equation A13 come from data runs such as that shown in Figure 1. The lifetimes  $\tau^{\text{on}}$  and  $\tau^{\text{off}}$  are obtained by fitting the decaying recombination and ionization signals with the Cooler on and off, respectively. For a given state of the Cooler, the recombination and ionization lifetimes agree to within their respective uncertainties. Here we use the lifetime measurement from the recombination data as it has better statistics than that derived from the ionization data. The lifetime fits are extrapolated to  $t_0$  in order to determine  $R_c^{1,\text{on}}$ ,  $R_c^{2,\text{on}}$ ,  $R_c^{1,\text{off}}$ , and  $R_c^{2,\text{off}}$ .

The accuracy for the inferred value of  $\hat{\alpha}$  as given by Equation A13 depends on the uncertainties in the various measured quantities on the right hand side of the equation. Here we assume that for any variable  $x$ , the error  $\sigma_x$  is uncorrelated with other variables. We took

partial derivatives to calculate  $\sigma_{\hat{\alpha}}$  in a linear approximation. We simplify the notation using  $R_c^{1,\text{on}}(t_0) \equiv R_{1,\text{on}}$ ,  $\eta_c \equiv \eta$ , etc. With the aid of MATHEMATICA, and after much algebraic manipulation, we find

$$\begin{aligned}
\sigma_{\hat{\alpha}}^2 = & \left\{ \left[ \eta^2 n^2 R_{2,\text{off}}^2 (R_{1,\text{off}} - R_{1,\text{on}} + R_{2,\text{off}} - R_{2,\text{on}})^2 (R_{1,\text{on}} R_{2,\text{off}} - R_{1,\text{off}} R_{2,\text{on}})^2 (\sigma_{\tau_{\text{off}}^{-1}}^2 + \sigma_{\tau_{\text{on}}^{-1}}^2) \right. \right. \\
& + R_{2,\text{off}}^2 (R_{1,\text{off}} - R_{1,\text{on}} + R_{2,\text{off}} - R_{2,\text{on}})^2 (R_{1,\text{on}} R_{2,\text{off}} - R_{1,\text{off}} R_{2,\text{on}})^2 (\sigma_{\eta}^2 n^2 + \sigma_n^2 \eta^2) (\tau_{\text{off}}^{-1} - \tau_{\text{on}}^{-1})^2 \\
& + \eta^2 n^2 R_{2,\text{off}}^2 (R_{2,\text{off}} - R_{2,\text{on}})^2 (R_{1,\text{on}} + R_{2,\text{on}})^2 \sigma_{R_{1,\text{off}}}^2 (\tau_{\text{off}}^{-1} - \tau_{\text{on}}^{-1})^2 \\
& + \eta^2 n^2 R_{2,\text{off}}^2 (R_{1,\text{off}} + R_{2,\text{off}})^2 (R_{2,\text{off}} - R_{2,\text{on}})^2 \sigma_{R_{1,\text{on}}}^2 (\tau_{\text{off}}^{-1} - \tau_{\text{on}}^{-1})^2 \\
& + \eta^2 n^2 (R_{1,\text{off}} R_{2,\text{on}} (-R_{1,\text{off}} - 2R_{2,\text{off}} + R_{2,\text{on}}) + R_{1,\text{on}} (R_{2,\text{off}} + R_{1,\text{off}} R_{2,\text{on}}))^2 \sigma_{R_{2,\text{off}}}^2 (\tau_{\text{off}}^{-1} - \tau_{\text{on}}^{-1})^2 \\
& \left. + \eta^2 n^2 (R_{1,\text{off}} - R_{1,\text{on}})^2 R_{2,\text{off}}^2 (R_{1,\text{off}} + R_{2,\text{off}})^2 \sigma_{R_{2,\text{on}}}^2 (\tau_{\text{off}}^{-1} - \tau_{\text{on}}^{-1})^2 \right] \\
& / \left[ \eta^4 n^4 R_{2,\text{off}}^4 (R_{1,\text{off}} - R_{1,\text{on}} + R_{2,\text{off}} - R_{2,\text{on}})^4 \right] \}. \tag{A14}
\end{aligned}$$

If detector 2 is not available, additional assumptions must be made, a discussion of which is beyond the scope of this paper.

To conclude we mention the special case described in Section 3.3 where the pressure in the Cooler does not change with switching the electron beam ( $\rho_c^{\text{on}} = \rho_c^{\text{off}}$ ) and the signal on detector 1 is dominated by electron induced processes ( $\alpha^1 \gg \beta^1$ ). Equation A13 then reduces to

$$\hat{\alpha} = \frac{\tau_{\text{on}}^{-1} - \tau_{\text{off}}^{-1}}{\eta n} \tag{A15}$$

where we have dropped the Cooler subscripts for convenience. This is equivalent to Equation 5. The associated error is given by

$$\sigma^2(\hat{\alpha}) = \frac{\sigma_{\tau_{\text{on}}^{-1}}^2 + \sigma_{\tau_{\text{off}}^{-1}}^2}{\eta^2 n^2} + \frac{(n^2 \sigma_{\eta}^2 + \eta^2 \sigma_n^2) (\tau_{\text{off}}^{-1} - \tau_{\text{on}}^{-1})^2}{\eta^4 n^4}. \tag{A16}$$

## B. List of abbreviations

CP collisionally ionized plasma

**DR** dielectronic recombination

**MCBP** multi-configuration Breit-Pauli

**MBRRC** merged-beams recombination rate coefficient

**PP** photoionized plasma

**PRRC** plasma rate coefficient

**RR** radiative recombination



## REFERENCES

- Altun, Z., Yumak, A., Badnell, N. R., Loch, S. D., & Pindzola, M. S. 2006, *A&A*, 447, 1165
- Altun, Z., Yumak, A., Yavuz, I., Badnell, N. R., Loch, S. D., & Pindzola, M. S. 2007, *A&A*, 474, 1051
- Arnaud, M., & Raymond, J. 1992, *ApJ*, 398, 394
- Badnell, N. R. 1986, *J. Phys. B*, 19, 3827
- . 2006a, *J. Phys. B*, 39, 4825
- . 2006b, *ApJ*, 651, L73
- . 2011, *Comp. Phys. Commun.*, 182, 1528
- Badnell, N. R., Foster, A., Griffin, D. C., Kilbane, D., O’Mullane, M., & Summers, H. P. 2011, *J. Phys. B*, 44, 135201
- Behar, E., Sako, M., & Kahn, S. M. 2001, *ApJ*, 563, 497
- Bryans, P., Badnell, N. R., Gorczyca, T. W., Laming, J. M., Mitthumsiri, W., & Savin, D. W. 2006, *ApJS*, 167, 343
- Bryans, P., Landi, E., & Savin, D. W. 2009, *ApJ*, 691, 1540
- Burgess, A. 1964, *ApJ*, 139, 776
- Chakravorty, S., Kembhavi, A. K., Elvis, M., Ferland, G., & Badnell, N. R. 2008, *Mon. Not. R. Astron. Soc.*, 384, L24
- Fawcett, B. C., Kononov, E. Y., Hayes, R. W., & Cowan, R. D. 1972, *J. Phys. B*, 5, 1255

- Grieser, M., Habs, D., von Hahn, R., Kleffner, C. M., Repnow, R., Stampfer, M., Jaeschke, E., & Steck, M. 1991, IEEE Particle Accelerator Conference, 5, 2817
- Gu, M. F. 2004, ApJS, 153, 389
- Gwinner, G., et al. 2000, Phys. Rev. Lett., 84, 4822
- Habs, D., et al. 1989, Nucl. Instrum. Methods B, 43, 390
- Hochadel, B., Albrecht, F., Grieser, M., Habs, D., Schwalm, D., Szmola, E., & Wolf, A. 1994, Nucl. Instrum. Methods B, 343, 401
- Hoffknecht, A., Schippers, S., Müller, A., Schwalm, D., & Wolf, A. 2001, Phys. Scr., T92, 402
- Holzner, T., Behar, E., & Arav, N. 2010, ApJ, 708, 981
- Hörndl, M., Yoshida, S., Wolf, A., Gwinner, G., Seliger, M., & Burgdörfer, J. 2006, Phys. Rev. A, 74, 052712
- Huang, K. 1984, At. Data Nucl. Data Tables, 30, 313
- Kaastra, J. S., & Mewe, R. 1993, Astron. Astrophys. Suppl. Ser., 97, 443
- Kallman, T. R. 2010, Space Sci. Rev., 157, 177
- Kilgus, G., Habs, D., Schwalm, D., Wolf, A., Badnell, N. R., & Müller, A. 1992, Phys. Rev. A, 49, 5730
- Kraemer, S. B., Ferland, G. J., & Gabel, J. R. 2004, ApJ, 604, 556
- Lampert, A., Wolf, A., Habs, D., Kenntner, J., Kilgus, G., Schwalm, D., Pindzola, M. S., & Badnell, N. R. 1996, Phys. Rev. A, 53, 1413

- Lestinsky, M. 2007, Dissertation, Universität Heidelberg,  
<http://www.ub.uni-heidelberg.de/archiv/7334/>
- Lestinsky, M., et al. 2008, *Phys. Rev. Lett.*, 100, 033001
- . 2009, *ApJ*, 698, 648
- . in preparation
- Linkemann, J., et al. 1995, *Nucl. Instrum. Methods B*, 98, 154
- Lukić, D. V., et al. 2007, *ApJ*, 664, 1244
- Martinson, I., & Gaupp, A. 1974, *Phys. Reports*, 15, 113
- Miersch, G., Habs, D., Kenntner, J., Schwalm, D., & A.Wolf. 1996, *Nucl. Instrum. Methods A*, 369, 277
- Müller, A. 1999, *Int. J. Mass Spectrom.*, 192, 9
- Netzer, H. 2004, *ApJ*, 604, 551
- Orlov, D. A., Weigel, U., Schwalm, D., Terekhov, A. S., & Wolf, A. 2004, *Nucl. Instrum. Methods A*, 532, 418
- Pastuszka, S., et al. 1996, *Nucl. Instrum. Methods A*, 369, 11
- . 2000, *J. Appl. Phys.*, 88, 6788
- Pedersen, H. B., et al. 2005, *Phys. Rev. A*, 72, 012712
- Pindzola, M. S., Griffin, D. C., & Bottcher, C. 1986, in *Atomic Process in Electron-Ion and Ion-Ion Collisions*, ed. F. Brouillard (Plenum), 75–91
- Poth, H. 1990, *Phys. Rep.*, 196, 135

- Ralchenko, Y., Kramida, A., Reader, J., & NIST ASD Team. 2011, Atomic Spectra Database, version 4.1.0, <http://physics.nist.gov/asd>, National Institute of Standards and Technology, Gaithersburg, MD.
- Rinn, K., Müller, A., Eichenauer, H., & Salzborn, E. 1982, *Rev. Sci. Instrum.*, 53, 829
- Sako, M., et al. 2001, *A&A*, 365, L168
- Schippers, S. 2009, *J. Phys.: Conf. Ser.*, 163, 012001
- Schippers, S., Lestinsky, M., Müller, A., Savin, D. W., Schmidt, E. W., & Wolf, A. 2010, *Int. Rev. Atom. Mol. Phys.*, 1, 109
- Schippers, S., Müller, A., Gwinner, G., Linkemann, J., Saghiri, A., & Wolf, A. 2001, *ApJ*, 555, 1027
- Schippers, S., Schnell, M., Brandau, C., Kieslich, S., Müller, A., & Wolf, A. 2004, *A&A*, 421, 1185
- Schmidt, E. W., et al. 2006, *ApJ*, 641, L157
- . 2008, *A&A*, 492, 265
- Shirai, T., Funatake, Y., Mori, K., Sugar, J., Wiese, W. L., & Nakai, Y. 1990, *J. Phys. Chem. Ref. Data*, 19, 127
- Sprenger, F., Lestinsky, M., Orlov, D. A., Schwalm, D., & Wolf, A. 2004, *Nucl. Instrum. Methods A*, 532, 298
- Steck, M., et al. 1990, *Nucl. Instrum. Methods A*, 287, 324
- Stobbe, M. 1930, *Ann. Phys.*, 399, 661

Träbert, E., Gwinner, G., Wolf, A., Knystautas, E. J., Garnir, H., & Tordoir, X. 2002, J. Phys. B, 35, 671

Wissler, G. 2002, Dissertation, Universität Heidelberg,  
<http://www.ub.uni-heidelberg.de/archiv/3101>

Wolf, A., & Gwinner, G. 2003, Hyperfine Interact., 146/147, 5

Wolf, A., et al. 2006, Hyperfine Interact., 172, 111

Table 1. Energy levels of Fe XII relative to the  $3s^2 3p^3 [^4S_{3/2}^o]$  ground level (Ralchenko et al. 2011) for excitations within the M-shell ( $\Delta N = 0$ ).

Level	Energy (eV)
$3s^2 3p^3 [^2D_{3/2}^o]$	5.1535
$3s^2 3p^3 [^2D_{5/2}^o]$	5.7126
$3s^2 3p^3 [^2P_{1/2}^o]$	9.1883
$3s^2 3p^3 [^2P_{5/2}^o]$	9.9826
$3s 3p^4 [^4P_{5/2}]$	34.0179
$3s 3p^4 [^4P_{3/2}]$	35.2121
$3s 3p^4 [^4P_{1/2}]$	35.7455
$3s 3p^4 [^2D_{3/2}]$	42.1571
$3s 3p^4 [^2D_{5/2}]$	42.3658
$3s 3p^4 [^2P_{3/2}]$	48.3174
$3s 3p^4 [^2S_{1/2}]$	48.8646
$3s^2 3p^2 (^1D) 3d [^2P_{3/2}]$	62.2153
$3s^2 3p^2 (^3P) 3d [^4P_{5/2}]$	63.5431
$3s 3p^4 [^2P_{1/2}]$	63.7093
$3s^2 3p^2 (^3P) 3d [^4P_{3/2}]$	64.0676
$3s^2 3p^2 (^3P) 3d [^4P_{1/2}]$	64.4433
$3s^2 3p^2 (^1S) 3d [^2D_{3/2}]$	65.2306
$3s^2 3p^2 (^1S) 3d [^2D_{5/2}]$	66.7085
$3s^2 3p^2 (^1D) 3d [^2D_{3/2}]$	68.6910
$3s^2 3p^2 (^1D) 3d [^2D_{5/2}]$	68.7629

Table 1—Continued

Level	Energy (eV)
$3s^2 3p^2 ({}^1D) 3d [{}^2P_{1/2}]$	70.5396
$3s^2 3p^2 ({}^3P) 3d [{}^2F_{5/2}]$	71.5066
$3s^2 3p^2 ({}^3P) 3d [{}^2P_{3/2}]$	71.6306
$3s^2 3p^2 ({}^1D) 3d [{}^2S_{1/2}]$	71.8650
$3s^2 3p^2 ({}^3P) 3d [{}^2F_{7/2}]$	72.0571
$3s^2 3p^2 ({}^3P) 3d [{}^2D_{5/2}]$	74.8778
$3s^2 3p^2 ({}^3P) 3d [{}^2D_{3/2}]$	75.0699

Table 2. Integrated DR rate coefficients for Fe XII. Here, the values in brackets give the  $1\sigma$  statistical errors for the last digit(s) shown.

Energy range (eV)	$\int \alpha_{\text{theo}}^{\text{DR}} dE$ ( $10^{-9} \text{ cm}^3 \text{ s}^{-1} \text{ eV}$ )	$\int \alpha_{\text{exp}}^{\text{DR}} dE$	$\kappa = \frac{\int \alpha_{\text{theo}}^{\text{DR}} dE}{\int \alpha_{\text{exp}}^{\text{DR}} dE}$
0.0135 – 0.45	1.86	5.29(2)	0.352(6)
0.45 – 5.5	10.84	14.22(2)	0.762(14)
5.5 – 15.0	3.41	4.61(1)	0.741(10)
15.0 – 24.5	2.81	3.70(2)	0.758(12)
24.5 – 36.0	4.20	5.11(1)	0.821(4)
36.0 – 42.0	1.20	1.89(1)	0.633(3)
42.0 – 46.0	0.98	1.57(1)	0.624(2)
46.0 – 53.0	2.32	2.59(1)	0.893(5)
53.0 – 59.0	3.62	2.58(1)	1.400(6)
59.0 – 66.0	14.04	8.30(1)	1.693(12)
66.0 – 75.0	0.21	0.44(1)	0.468(3)
75.0 – 217.0	3.51	5.16(3)	0.680(20)
330.0 – 885.0	1.89	6.7(2)	0.282(51)



Table 3. Fit parameters  $c_i$  ( $\text{cm}^3 \text{s}^{-1} \text{K}^{3/2}$ ) and  $E_i$  (K) for the experimental DR PRRC for Fe XII using Equation 7.

$i$	$c_i$	$E_i$
1	$1.38 \times 10^{-3}$	$9.48 \times 10^2$
3	$5.18 \times 10^{-3}$	$5.61 \times 10^3$
4	$1.33 \times 10^{-2}$	$1.92 \times 10^4$
2	$2.23 \times 10^{-2}$	$6.14 \times 10^4$
5	$9.52 \times 10^{-2}$	$2.70 \times 10^5$
6	$2.29 \times 10^{-1}$	$8.28 \times 10^5$
7	$2.94 \times 10^{-1}$	$4.90 \times 10^6$

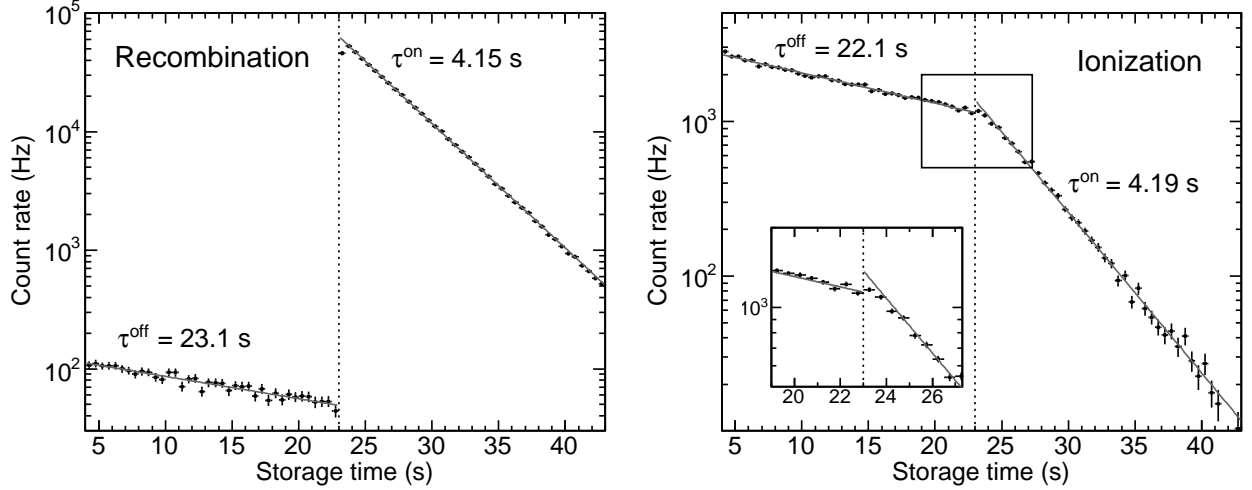


Fig. 1.— Count rates versus storage time measured with the Cooler recombination and ionization detectors, left and right, respectively. The Cooler beam was on for  $t = 0 - 3$  s, off for  $3 - 23$  s, and switched back on at  $t_0 = 23$  s. During the on-phase, we matched the electron and ion velocities ( $\hat{E} = 0$ ). Data were not acquired during precooling ( $t \leq 3$  s). The thin solid lines indicate the exponential fits used to derive the ion beam lifetimes  $\tau^{\text{off}}$  and  $\tau^{\text{on}}$ . The dotted vertical lines mark  $t_0$ . The inset in the right panel shows the increase of the ionization signal after switching on the Cooler beam which causes an increase in the residual gas pressure. Extrapolations of the solid lines to  $t_0$  were used to determine  $R_c^{1,\text{on}}$ ,  $R_c^{2,\text{on}}$ ,  $R_c^{1,\text{off}}$ , and  $R_c^{2,\text{off}}$ . See Appendix A for details.

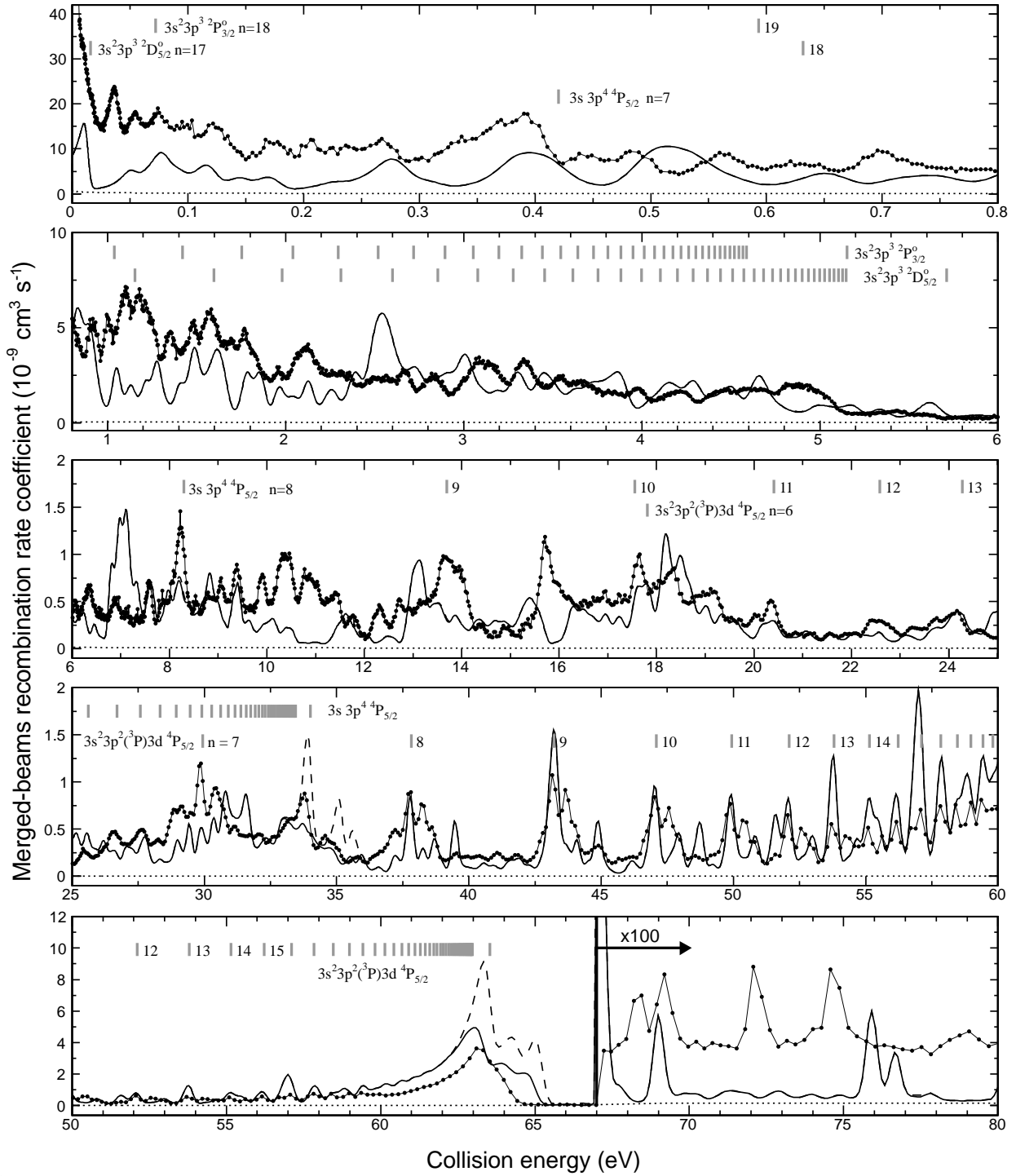


Fig. 2.— Caption on next page!

**Caption for Figure 2** MBRRC for Fe XII forming Fe XI as a function of relative collision energy. The data measured at the Cooler are shown by the connected solid points. The theoretical AUTOSTRUCTURE results with field ionization are shown by the solid line. Including the high  $n$  contributions missing due to field ionization gives the dashed line. The theoretical RR MBRRC is shown by the dotted line (on this scale it is almost compatible with zero at most collision energies). For clarity, we show the DR resonance energies associated with only four of the many possible Rydberg DR series (short vertical lines). We label those series by the corresponding core excitation configuration. In each series, the highest energy vertical mark corresponds to the series limit and the penultimate mark to the approximate field ionization cut-off.

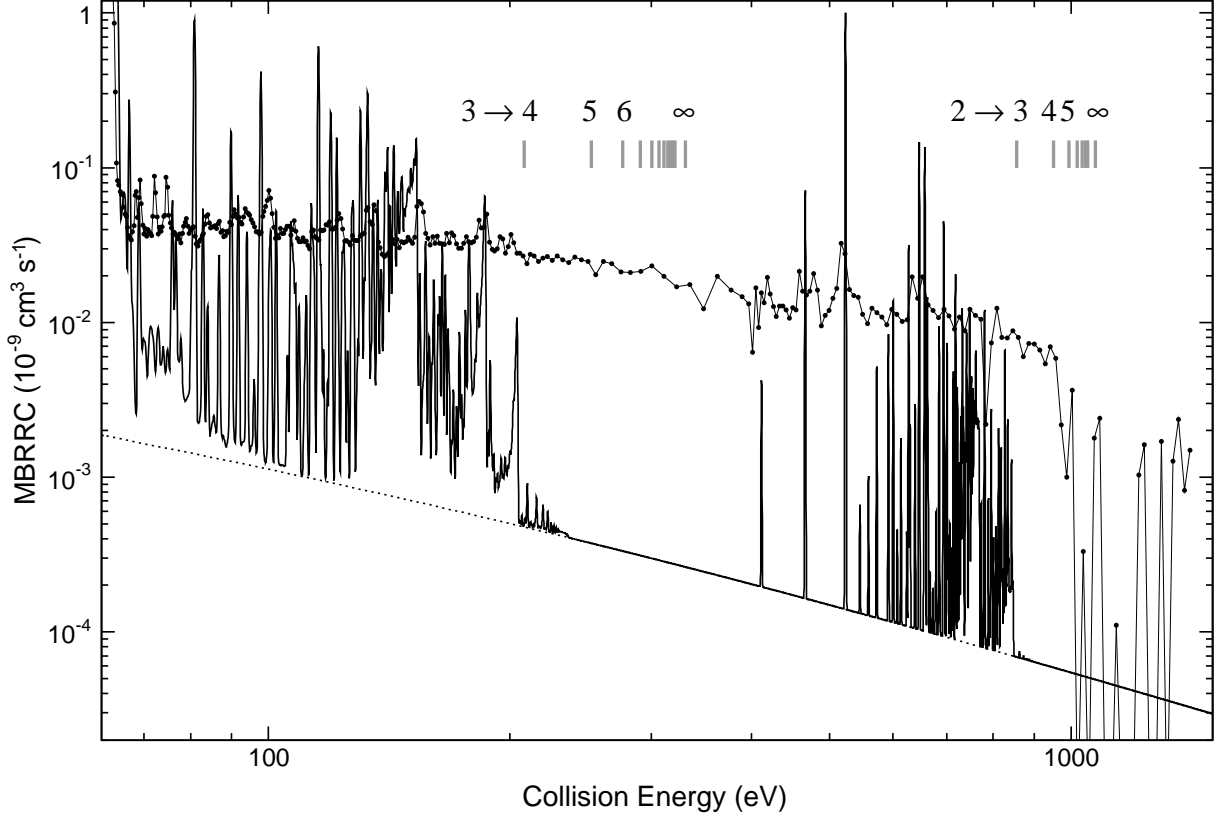


Fig. 3.— Same as Figure 2 but for collision energy ranges dominated by  $\Delta N > 0$  transitions. The short vertical lines mark the DR series limits for  $3 \rightarrow N'$  and  $2 \rightarrow N'$  core excitations as calculated by using a hydrogenic approximation, assuming hydrogenic Rydberg levels on a  $3s^2 3p^2$  core (labeled  $3 \rightarrow N'$ ) and on a  $2s^2 2p^5 3s^2 3p^3$  core (labeled  $2 \rightarrow N'$ ). No difference is seen between the calculations with and without the field ionization effects included. A significant amount of the measured DR flux is due to channels not accounted for in the theoretical calculations.

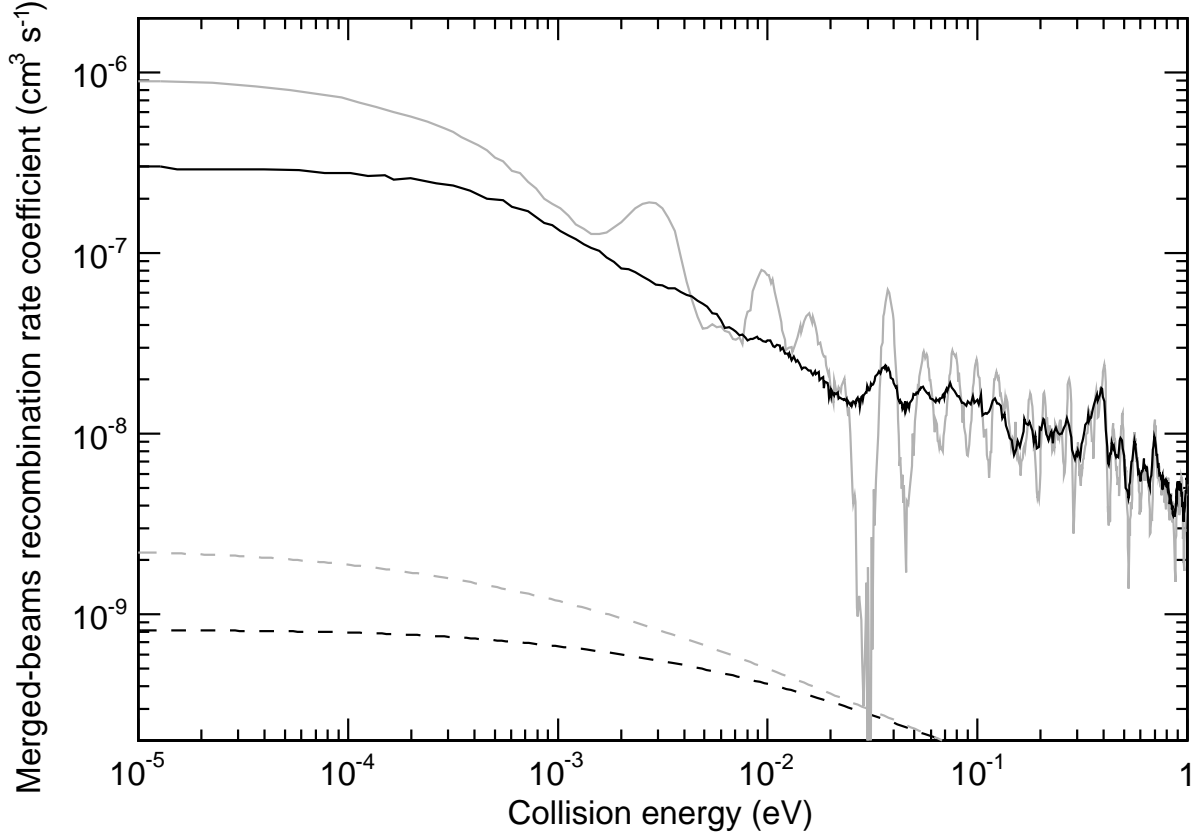


Fig. 4.— Comparison of the low energy Fe XII to Fe XI MBRRC data acquired at the Cooler (black full line,  $k_{\text{B}}T_{\perp}^{\text{c}} \approx 13.5$  meV) and at the Target (gray full line,  $k_{\text{B}}T_{\perp}^{\text{t}} \approx 1.5$  meV). The dashed lines show the theoretical RR contribution convolved with the electron energy spreads of the Cooler (black) and Target (gray), respectively.

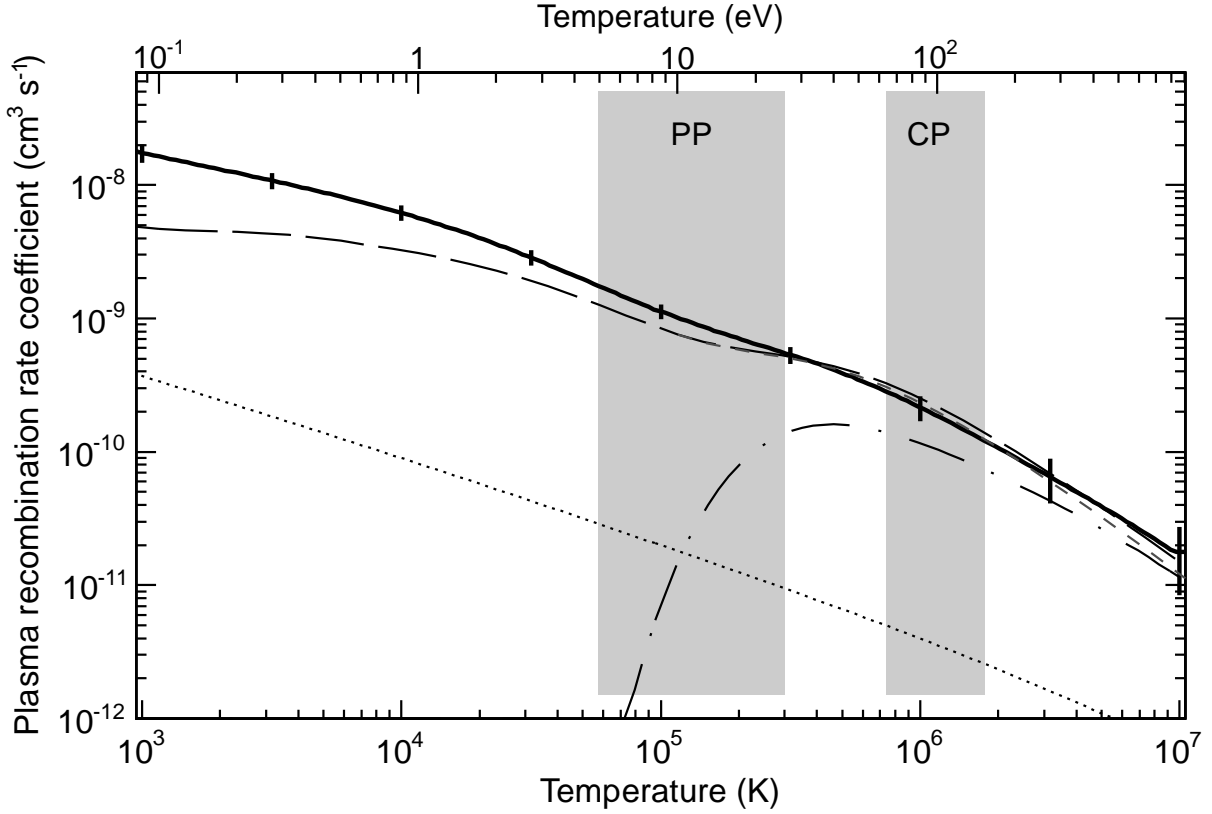


Fig. 5.— Comparison of the experimental and theoretical DR PRRC for Fe XII forming Fe XI. The thick solid line gives the experimental results and the error bars the experimental uncertainty at a  $1\sigma$  confidence level. The previously recommended rate coefficient of Arnaud & Raymond (1992) is shown by the long-dash-dotted curve. The short dashed curve gives previous results of Badnell (2006b) while the long dashed curve presents our new results which extend these older calculations by including  $N = 3 \rightarrow 4$  and  $2 \rightarrow 3$  core excitations. These two curves overlap below  $\sim 3 \times 10^5$  K. For comparison we plot also the calculated RR PRRC (dotted line) of Badnell (2006b). The shaded areas indicate the plasma temperatures where the Fe XII abundance is  $\geq 1\%$  in photoionized plasmas (PP; Kallman 2010) and in collisionally ionized plasmas (CP; Bryans et al. 2006, 2009).